Available online at www.sciencedirect.com
ScienceDirect
Computers & Fluids 36 (2007) 238–247
computers & fluids
www.elsevier.com/locate/compfluid

Pseudo-spectral numerical simulation of miscible fluids with a high density ratio

Y. Jang, S.M. de Bruyn Kops *

Department of Mechanical and Industrial Engineering, University of Massachusetts Amherst, 160 Governors Drive, Amherst, MA 01003, USA

Received 8 August 2005; received in revised form 10 October 2005; accepted 15 November 2005
Available online 14 February 2006

Abstract

A computational algorithm is described for direct numerical simulation (DNS) of turbulent mixing of two incompressible miscible fluids having greatly differing densities. The algorithm uses Fourier pseudo-spectral methods to compute spatial derivatives and a fractional step method involving the third-order Adams–Bashforth–Moulton predictor–corrector scheme to advance the solution in time. The pressure projection technique is shown to eliminate stability problems, previously observed, when the ratio of the densities in the two streams is as high as 35. The algorithm is investigated in detail for mixing in isotropic homogeneous turbulence of two fluids with a density ratio of 10. The limit on the density ratio is imposed so that the flow is both everywhere turbulent and spatially resolved. Both fluids have the same molecular viscosities, the nominal Schmidt number is 0.7, and the initial nominal Reynolds number based on the integral length scale and the rms velocity is 158. No body force is considered. It is shown that the pressure projection scheme does not limit the temporal accuracy of the solution when periodic boundary conditions are used, but that it significantly affects the stability of the simulations. It is also shown that the rate at which turbulence kinetic energy dissipates averaged for the whole computational domain is almost unaffected by density ratio.

1. Introduction

Since the seminal laboratory experiments in variable density turbulence by Brown and Roshko [1], considerable progress has been made toward understanding and modeling flows in which large density variations are the result of temperature or concentration gradients. Nevertheless, Lele [2] recently concluded that "new experiments (laboratory and numerical) which are specifically designed to shed light on physical and modeling issues, and executed in conjunction with theoretical and modeling studies are critical for further advances". Similarly, Belan [3] notes that more extensive data sets are necessary for validating variable density turbulence models. Brown and Roshko [1] remark that laboratory experiments in variable density turbulence are quite difficult due to the fact that either a wide temperature range is required to produce the desired density gradient, or else bottled gases must be used, which are not free. It is informative that Brown and Roshko could afford to run their experiments for several seconds whereas experiments in constant density turbulence are often run for hours while equipment equilibrates and conditions are adjusted to produce as nearly canonical flows as possible. While experimental techniques have improved significantly since Brown and Roshko conducted their experiments, the problem of generating a high density ratio persists. This suggests that, for studying cannonical flows for the purpose of theory and model development, direct numerical simulations are a valuable tool.

In direct numerical simulations, the Navier–Stokes equations and other transport equations of interest are numerically solved on a computational grid sufficiently fine to resolve all the scales of turbulent motion [4]. If the appropriate equations are solved accurately and with suitable initial and boundary conditions, it is often argued that the results can be used in the development and testing of

* Corresponding author. Tel.: +1 413 545 0206; fax: +1 413 545 1027.
E-mail address: debk@acad.umass.edu (S.M. de Bruyn Kops).

0045-7930/$ - see front matter © 2005 Elsevier Ltd. All rights reserved.
doi:10.1016/j.compfluid.2005.11.003

models and theories on turbulent flows. Orszag and Patterson [5] presented the first DNS results to show a simulated flow field with many of the characteristics of a turbulent flow. In the subsequent decade, the technique was employed to study, e.g., first-order closure modeling [6,7], density stratified flows [8,9], and turbulent wakes [10]. As computing power increased, turbulent reacting flows became the focus of many DNSs because the simulations could provide information at length and time scales difficult to measure in the laboratory [11–13]; Vervisch and Poinsot [14] provide a review. Recent direct numerical simulations have also been used to study flows in which density gradients are due to high Mach number effects, i.e., compressible flows, including channel flow [15,16], boundary layers [17,18], shear layers [19], and jets [20,21].

The term *variable density turbulence* takes on different meanings depending on context. For aeronautics, it is usually taken to refer to flows in which density differences are due to high Mach number effects. For geophysical fluid dynamics, variable density turbulence is often considered within the restrictions of the Boussinesq approximation. In this paper, we consider turbulent interaction of two miscible incompressible fluids with differing densities and denote this flow regime as variable density at zero Mach number (VDZM).

The mathematical foundation for the zero Mach number methodology is provided by Klainerman and Majda [22]. McMurtry et al. [23,24] employed it in their studies of a chemically reacting mixing layer, and Cook and Riley [12] used a similar approach to simulate a reacting plume. Sandoval [25] develops the equations of motion for incompressible miscible fluids having differing densities, and solves them numerically with a density ratio of 4. All of these researchers found that the explicit numerical schemes used to advance the zero Mach number equations in time were unstable except for fairly low density ratios. To avoid this problem, Najm et al. [26] implement a predictor–corrector scheme for simulations of reacting flows, and Cook and Dimotakis [27] use a slightly different predictor–corrector scheme to simulate Rayleigh–Taylor instabilities with a density ratio of three. The latter formulation, however, is still not suitable for density ratios up to 35 typical of recent laboratory experiments, e.g., [28–34].

It is important to note that the difficulties that researchers have had in running simulations with high density ratios are due to the use of spectral methods to compute the spatial derivatives. Spectral methods are very attractive for numerical investigations of basic physics because phase errors are very small, rates of convergence are very high, and the truncation error decreases faster than algebraically as the number of Fourier modes becomes large [35]. Practical implementation of spectral methods, however, requires the use of an explicit time stepping scheme. If, for instance, a finite volume technique were used then a left-hand side matrix with variable coefficients could be used to overcome the numerical issues discussed here.

In this paper, we address numerical issues associated with using pseudo-spectral methods to simulate miscible fluids with high density ratios and present an algorithm that has been tested satisfactorily for density ratios as high as 35. The equations governing variable density miscible flows at zero Mach number are reviewed in the next section, and an explicit numerical method for solving these equations with high density ratios is developed in Section 3. In Section 4, we present the flow configuration used for our tests of the algorithm. In Section 5, computational issues are considered, including temporal accuracy, pressure projection, and dealiasing. Some modeling implications of the simulation results for isotropic homogeneous turbulence with high density ratio are discussed in Section 6.

2. Formulation

The flow of two miscible fluids is assumed to be a solution to the non-dimensional Navier–Stokes equations

$$\frac{\partial \rho}{\partial t} + \frac{\partial \rho u_j}{\partial x_j} = 0, \tag{1}$$

$$\frac{\partial \rho u_i}{\partial t} + \frac{\partial \rho u_i u_j}{\partial x_j} = -\frac{\partial p}{\partial x_i} + \frac{\partial \tau_{ij}}{\partial x_j} + \frac{1}{F^2}\rho g_i. \tag{2}$$

Additionally, assuming Fickian diffusion and no interfacial surface tension, the transport equation for Y_i, the mass fraction of species i(=1 or 2), is

$$\frac{\partial \rho Y_i}{\partial t} + \frac{\partial \rho u_j Y_i}{\partial x_j} = \frac{1}{Pe}\frac{\partial}{\partial x_j}\left(\rho \frac{\partial Y_i}{\partial x_j}\right). \tag{3}$$

Here, $\rho(x_i, t)$, $u_i(x_i, t)$, and $p(x_i, t)$ are the density, velocity, and pressure fields, and g_i is the acceleration vector. Eqs. (1)–(3) have been non-dimensionalized by characteristic velocity and length scales U and L, an acceleration magnitude g, and by a characteristic density ρ_0 taken here to be the (constant) mean density in the flow. The dynamic viscosity μ and the mass diffusivity $\mathscr{D}$ are assumed to be the same for both species so that the nominal Reynolds number, $Re = UL\rho_0/\mu$, and the nominal Péclet number, $Pe = UL\rho_0/\mathscr{D}$, are constant. $F = \sqrt{U^2/gL}$ is a Froude number. For the viscous stresses, a Newtonian fluid with zero dilatational viscosity, e.g., an ideal monoatomic gas, is assumed so that

$$\tau_{ij} = \frac{1}{Re}\left[\frac{\partial u_i}{\partial x_j} + \frac{\partial u_j}{\partial x_i} - \frac{2}{3}\delta_{ij}\frac{\partial u_n}{\partial x_n}\right]. \tag{4}$$

Denoting the (constant) microscopic densities of the two species as ρ_1 and ρ_2, the local density is related to the mass fractions by

$$\frac{1}{\rho} = \frac{Y_1}{\rho_1} + \frac{Y_2}{\rho_2}. \tag{5}$$

Combining (1) and (3) and noting that $Y_1 + Y_2 = 1$ yields an equation for the evolution the local density (cf. [36,29,37,28,25,27])

$$\frac{\partial \rho}{\partial t} + u_j \frac{\partial \rho}{\partial x_j} = \frac{\rho}{Pe} \frac{\partial}{\partial x_j}\left(\frac{1}{\rho}\frac{\partial \rho}{\partial x_j}\right) \tag{6}$$

and an equation for the divergence of the velocity field

$$\frac{\partial u_j}{\partial x_j} = -\frac{1}{Pe}\frac{\partial}{\partial x_j}\left(\frac{1}{\rho}\frac{\partial \rho}{\partial x_j}\right). \tag{7}$$

So while the flow is composed of two incompressible fluids, the velocity field is divergent.

In the preceding derivation, several important restrictions have been applied. By assuming Fickian diffusion, we implicitly assume that mass diffusion due to temperature and pressure gradients is negligible compared with that resulting from concentration gradients. Thus, the flow is assumed to be at zero Mach number so that fluctuations in temperature and pressure are small compared with their mean values. Additionally, ρ_1 and ρ_2 are constant so that each fluid is incompressible and the thermal energy equation is decoupled from the problem.

3. Numerical algorithm

Eqs. (2) and (6) with appropriate boundary conditions constitute a well posed problem that is to be solved numerically. In particular, we are interested in highly accurate solutions to canonical flow configurations for use in developing theories and models for VDZM turbulence. Since spectral methods have the advantages for this application that are noted in the introduction, we consider a numerical domain that is a cube with periodic or free-slip boundary conditions in all directions, and use a pseudo-spectral method for spatial discretization.

The governing equations are integrated in time from t^n to $t^{n+1} = t^n + \Delta t$ using a fractional step method involving third-order Adams–Bashforth–Moulton discretization in time and a first-order pressure projection step. The method is similar to but different from those of Najm et al. [26] and Cook and Dimotakis [27]. The solution procedure involves first predicting the density at time t^{n+1} along with the half-step momentum, which does not include the pressure term. A Poisson equation is then solved for the pressure effect and the predicted momentum at t^{n+1} is formed. The corrected density and half-step momentum are then computed, followed by a corrected pressure projection. The steps of the solution method are outlined below.

3.1. Predictor step

In the predictor step, estimates for the density and momentum at t^{n+1} are computed using a second-order Adams–Bashforth time integration scheme and denoted by the superscript $\mathscr{P}$. The superscript $*$, often used to indicate a predicted quantity, is reserved to denote the half-step momentum. We begin by writing the density equation (6), in terms of the natural log of density in order to simplify computation of the diffusion term using spectral methods:

$$\frac{\partial \rho}{\partial t} = \rho\left(\frac{1}{Pe}\nabla^2 \log\rho - \boldsymbol{u}\cdot\nabla\log\rho\right). \tag{8}$$

It is not desirable to advance $\log\rho$ in time, however, since doing so would cause the numerical errors to be amplified when the exponential it taken to recover ρ. So the predicted density is

$$\rho^{\mathscr{P}} = \rho^n + \frac{\Delta t}{2}(3R_\rho^n - R_\rho^{n-1}), \tag{9}$$

where

$$R_\rho = \rho\left(\frac{1}{Pe}\nabla^2 \log\rho - \boldsymbol{u}\cdot\nabla\log\rho\right). \tag{10}$$

During the first time step of the simulation, R_ρ^{n-1} is not known, so that the Adams–Bashforth scheme is not suitable for the solution of $\rho^{\mathscr{P}}$. For the first time step, a forward Euler scheme is used:

$$\rho^{\mathscr{P}} = \rho^n + (\Delta t)R_\rho^n. \tag{11}$$

Next, the half-step momentum, $\boldsymbol{m}^*$, is computed by advancing the viscous, body force, and nonlinear terms in time:

$$\boldsymbol{m}^* = \rho\boldsymbol{u}^n + \frac{\Delta t}{2}[3R^n - R^{n-1}], \tag{12}$$

where $R = \nabla\cdot\boldsymbol{\tau} + \rho\boldsymbol{g} - \nabla\cdot(\rho\boldsymbol{u}\boldsymbol{u})$. The predicted hydrodynamic pressure is determined by inverting the Poisson equation

$$\nabla^2 p^{\mathscr{P}} = \frac{1}{\Delta t}\left[\nabla\cdot\boldsymbol{m}^* + \left.\frac{\partial\rho}{\partial t}\right|^{\mathscr{P}\mathscr{P}}\right]. \tag{13}$$

McMurtry [38] was apparently the first to note that error in predicting $(\partial\rho/\partial t)^{\mathscr{P}}$ in (13) is the source of the numerical instability observed by various researchers when solving the zero Mach number equations. Continuity can be used to replace the term with $-\nabla\cdot(\rho\boldsymbol{u})^{\mathscr{P}}$, in which case it is apparent that (2) and (13) can be solved simultaneously via block LU decomposition as recommended for incompressible flows by Perot [39]. Doing so, however, is impractical with pseudo-spectral spatial discretization, and so we assume

$$\left.\frac{\partial\rho}{\partial t}\right|^{\mathscr{P}} = (2.1R_\rho^n - 1.2R_\rho^{n-1} + 0.1R_\rho^{n-2}) \tag{14}$$

justification for which is presented in Section 5.4. Then

$$(\rho\boldsymbol{u})^{\mathscr{P}} = \boldsymbol{m}^* - \Delta t\nabla p^{\mathscr{P}} \tag{15}$$

and we recover the velocity by assuming that $\rho^{\mathscr{P}}\boldsymbol{u}^{\mathscr{P}} = (\rho\boldsymbol{u})^{\mathscr{P}}$.

3.2. Corrector step

The corrected density at time step $n+1$ is obtained using the third-order Adams–Moulton corrector, i.e.,

$$\rho^{n+1} = \rho^{\mathscr{P}} + \frac{5\Delta t}{12}(R_\rho^{\mathscr{P}} - 2R_\rho^n + R_\rho^{n-1}). \tag{16}$$

A trapezoid corrector is used for the first time step.

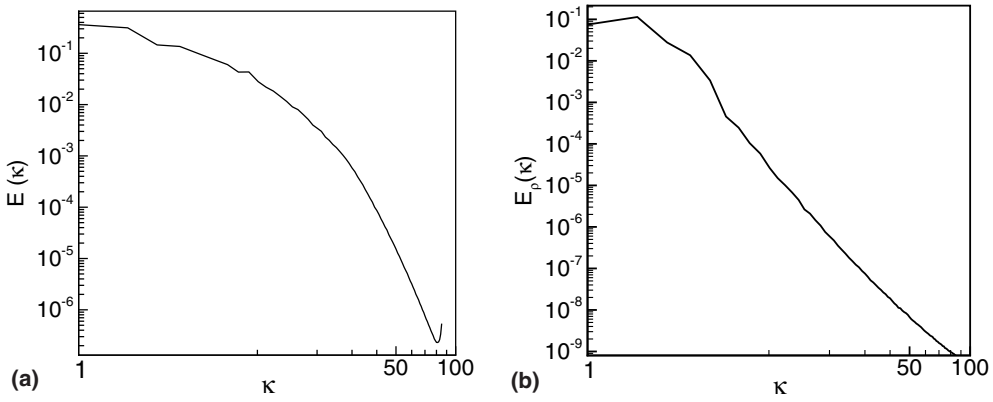

Fig. 1. Initial velocity and density energy spectra for $r = 10$.

The momentum at t^{n+1} is computed from

$$\boldsymbol{m}^{**} = \rho^{\mathscr{P}}\boldsymbol{u}^{\mathscr{P}} + \frac{5\Delta t}{12}\left[R^{\mathscr{P}} - 2R^{n} + R^{n-1}\right] \tag{17}$$

and

$$\nabla^2 p^{n+1} = \frac{1}{\Delta t}\left[\nabla\cdot\boldsymbol{m}^{**} + \left.\frac{\partial\rho}{\partial t}\right|^{n+1}\right]. \tag{18}$$

Here, $(\partial\rho/\partial t)^{n+1}$ is estimated from (6) using ρ^{n+1} and $\boldsymbol{u}^{\mathscr{P}}$. Finally,

$$(\rho\boldsymbol{u})^{n+1} = \boldsymbol{m}^{**} - \Delta t\nabla p^{n+1} \tag{19}$$

and the assumption $\boldsymbol{u}^{n+1} = (\rho\boldsymbol{u})^{n+1}/\rho^{n+1}$ is made.

4. Flow configuration

To test the algorithm and investigate certain aspects of VDZM turbulence, we consider the case of decaying isotropic homogeneous turbulence. The initial velocity field is based on Nilsen and Kosály's (NK) simulations of an incompressible flow [40] (cf. [41]). Their simulations exhibited many characteristics of grid turbulence, but it is noted that matching results from actual laboratory experiments requires significantly greater large-scale resolution than was available to those authors at the time the simulations were run [42,43]. For the purposes of the current research, it is advantageous to start with the NK fields since they have been studied extensively and are relatively small and thus easy to work with. Sandoval et al. [25,44] used a substantially similar incompressible velocity field as the basis for his VDZM simulations.

The velocity field used as the basis for our initial conditions is the NK case R3. Defining ℓ as the integral length scale, u_{rms} as the rms of the fluctuating velocity, η_k as the Kolmogorov length scale, and ρ_0 as the mean density then $Re_\ell = u_{\mathrm{rms}}\ell\rho_0/\mu = 158$, $\ell/\eta_k = 44$ and $u_{\mathrm{rms}}/\ell = 1.02$. In a domain of length 2π on each side, the small scales of the field would be marginally resolved in a domain with 54 wave numbers per the criteria of Eswaran and Pope [45]. The NK velocity field was modified to create the initial conditions for the current simulations by imposing an initial density field (discussed below) and applying pressure projection so that $\nabla\cdot\rho\boldsymbol{u} = 0$. The initial velocity spectrum for density ratio $r = 10$ is shown in Fig. 1.

Fig. 2. Contour plot of initial mass fraction field Y_1.

The initial scalar fields are randomly generated in Fourier space using the method of Eswaran and Pope [45]. The fields are statistically isotropic with the integral length of the scalar comparable to the integral length of the velocity. A contour plot of the initial mass fraction field Y_1 is shown in Fig. 2, where Y_1 is related to ρ by

$$Y_1 = \frac{\rho_1(\rho - \rho_2)}{\rho(\rho_1 - \rho_2)}. \tag{20}$$

A density field with a specific density ratio is produced by selecting ρ_1 and ρ_2. For convenience, we use $\rho_0 = (\rho_1 + \rho_2)/2 = 1$, and μ is held constant, so that the nominal initial Reynolds number is the same for all cases and set equal to the initial Reynolds number in the NK simulations, i.e., $Re_\ell|^{t=0} = 158$. Simulations with r as high as 35 have been run successfully to show that the algorithm is capable of simulating density ratios comparable to those currently being studied in the laboratory, but the $r = 10$ case is presented in this paper for the following reasons. In the $r = 10$ case, $\rho_1 = 1/0.55$ and $\rho_2 = 1/5.5$, so the initial Reynolds number in the low density fluid is 29, which, based on

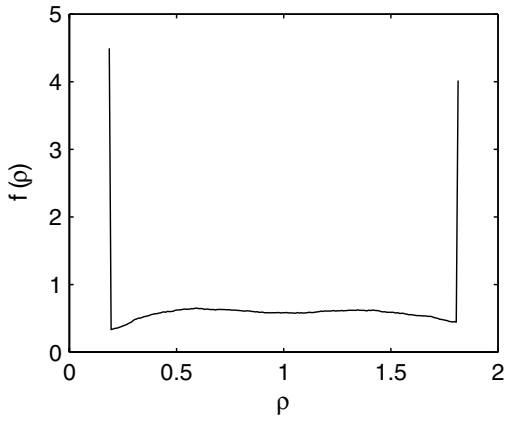

Fig. 3. Probability density function of the initial density field with $r = 10$.

studies of the incompressible case, is marginally turbulent. The initial Reynolds number in the high density fluid is 287 which is near the highest that can be spatially resolved using a numerical domain with 256^3 grid points, again based on results from incompressible simulations with the NK initial velocity field. Thus, while the algorithm is stable for higher values of r, $r = 10$ is about the limit at which the flow is turbulent everywhere and spatially resolved. The scalar energy spectrum and probability density function of the initial density field with $r = 10$ are shown, respectively, in Figs. 1 and 3.

5. Numerics

In order to investigate the characteristics of the algorithm, a baseline simulation was developed in which errors due to temporal and spatial resolution and aliasing are negligible. This baseline case is denoted "V1" in Table 1. In this section are discussed the tests conducted to ensure this case is accurate. In the process, various characteristics of the algorithm are presented.

5.1. Local accuracy checks

Since the baseline simulation (case V1) was designed primarily to investigate the numerical algorithm presented in this paper, it does not require the full computational resources available. Consequently, it was possible to perform classical resolution tests by increasing spatial resolution and decreasing the time step until a converged solution was achieved. By comparing the value of the local velocity, $\boldsymbol{u}$, at several locations in simulations with differing grid spacings and time step sizes, case V1 was determined to be well resolved.

Table 1
Summary of simulation cases. r, N, and k_c/k_{max} are the density ratio, the number of grid points in each dimension, and the ratio of the cutoff wave number to the maximum wave number, respectively

Case	Re_ℓ	r	N	k_c/k_{max}
C1	29	1	128	0.9375
C2	158	1	192	0.9375
C3	287	1	256	0.9375
V1	158	10	192	0.9000
V2	158	35	512	0.9000

Case V1 was also run with other values of k_c/k_{max} to test for aliasing errors as discussed in Section 5.3.

5.2. Global conservation checks

In the algorithm, the continuity equation (1) is replaced by the transport equation for density (6) that describes the mixing of two miscible, incompressible fluids. As a result, simulations that are not adequately resolved in space and time will not necessarily conserve mass or momentum. In fact, it was observed in the process of developing the current simulations that conservation errors are detectable in a poorly resolved simulation long before instabilities occur. For the current simulations, the algorithm was found to conserve mass and momentum globally. In addition, the mechanical energy equation

$$\frac{\partial}{\partial t}\left(\frac{1}{2}\rho u_i^2\right) + \frac{\partial}{\partial x_j}\left(u_j \frac{1}{2}\rho u_i^2\right) = -u_i \frac{\partial p}{\partial x_i} + \rho u_i g_i + u_i \frac{\partial \tau_{ij}}{\partial x_j} \tag{21}$$

and the transport equation for the variance of the density fluctuations about ρ_0

$$\frac{\partial \rho'^2}{\partial t} + u_j \frac{\partial \rho'^2}{\partial x_j} = \frac{1}{Pe}\left[\frac{\partial}{\partial x_j}\left(\frac{\partial \rho'^2}{\partial x_j}\right) - \chi\left(1 + \left(\frac{\rho'}{\rho}\right)\right)\right], \tag{22}$$

with $\chi = 2\nabla\rho' \cdot \nabla\rho'$ were integrated at instants in time over the entire computational domain and checked that all terms that should be zero were zero and that the remaining terms balanced to machine precision. It was found that, for the proposed algorithm, testing that (21) and (22) balance is as strict a check of resolution as the point-wise tests, and can be used for problems that use all available computing capacity, i.e., when it is not practicable to increase the size of the computation domain or reduce the time step size for the purpose of testing resolution.

5.3. Dealiasing

Removal of all aliasing errors can be achieved in a pseudo-spectral simulation by filtering, i.e., by zeroing the Fourier coefficients for all wave numbers with magnitude greater than some cutoff wave number, k_c. In a simulation having N grid points, the maximum wave number is $k_{max} = N/2$. Orszag [46] showed that setting $k_c \leqslant 2/3 k_{max}$ will remove all aliasing in simulations involving quadratic nonlinear terms. In the current algorithm, the nonlinear terms involve three factors. To develop the theoretical dealiasing requirement for this case, let $x_j = 2\pi j/N$ for $j = 0, 1, \ldots, N-1$. Without loss of generality it is convenient to consider a domain of size 2π so that the wave numbers are integers and the truncated Fourier series for each factor in the nonlinear term are

$$\rho_j = \sum_{m=-M/2}^{M/2-1} \hat{\rho}_m e^{imx_j}$$
$$u_j = \sum_{n=-M/2}^{M/2-1} \hat{u}_n e^{inx_j} \quad (23)$$
$$v_j = \sum_{p=-M/2}^{M/2-1} \hat{v}_p e^{ipx_j}$$

where $M/2 = k_c$ and the symbol $\hat{}$ denotes a variable in Fourier space. The discrete transform of the product $z_j = \rho_j u_j v_j$ is

$$\hat{z}_k = \sum_{j=-M/2}^{M/2-1} z_j e^{-ikx_j}, \quad k = \frac{N}{2}, \ldots, \frac{N}{2} - 1. \quad (24)$$

Substituting (23) into (24) and omitting terms that are zero due to orthogonality

$$\hat{z}_k = \sum_{m+n+p=k} \hat{\rho}_m \hat{u}_n \hat{v}_p + \sum_{m+n+p=k\pm N} \hat{\rho}_m \hat{u}_n \hat{v}_p. \quad (25)$$

The second term on the right-hand side is the aliasing error. If we filter so that $\hat{\rho}_m, \hat{u}_m$, and $\hat{v}_m$ are zero for $|m| > M/2$ before the product is computed and $\hat{z} = 0$ for $|k| > M/2$ after the product is computed, then the largest value of M required to make the aliasing term zero occurs when $m = n = p = -M/2$ and $k = M/2 - 1$, i.e.,

$$-\frac{M}{2} - \frac{M}{2} - \frac{M}{2} \leqslant \frac{M}{2} - 1 - N \quad (26)$$

or

$$M \leqslant \frac{N+1}{2}. \quad (27)$$

So Orszag's 2/3 rule becomes the 1/2 rule for the current algorithm.

Since truncating half the wave numbers in each of three dimensions is prohibitively expensive, we consider alternative approaches. Patterson and Orszag [47] used phase shifting to reduce aliasing effects, as did Rogallo et al. [48–50], but implementing such a scheme on modern parallel computers incurs considerable cost. Kerr [51] reports that alternating between the conservation and convection forms when advancing a scalar transport equation in time causes most of the aliasing errors to cancel. More generally, solving an equation in skew-symmetric form significantly reduces aliasing errors [52,53]. However, computing (8) in conservation form is undesirable since it counteracts the simplifying effect of writing the equation in terms of $\log \rho$. Similarly, using the skew-symmetric form for the momentum equation significantly increases the cost of the simulation.

Blaisdell et al. [53] suggest that using the skew-symmetric form may be worthwhile for large-eddy simulations in which, by definition, all the length scales of turbulent motion are not resolved, but may not be necessary for direct numerical simulations that are well resolved. Additionally, McMurtry [38] states that the most damaging aliasing errors are removed in a direct numerical simulation with a quadratic nonlinear term if $k_c/k_{max} < 15/16$ and Sandoval [25] uses $k_c/k_{max} < 9/10$ for a nonlinear term with three products but does not show how this value was determined.

We seek here the largest value of k_c/k_{max} that will result in negligible aliasing errors. Having previously determined that the simulation is stable and conserves mass, momentum, and mechanical energy with $k_c = 86$, we examine a series of simulations with a range of grid sizes and $k_c = 90$; 90 is used instead of 86 in this phase of the testing to accommodate the requirement of FFT routines that values of N with small prime factors be used. The initial conditions for this series of simulations is case V1 at $t = 1$. The case of $k_{max} = 180$ meets the 1/2 rule and is used as the baseline against which the other cases are compared. Cases with $k_{max} = 90$, 96, 100, 108, 112, 128, and 192 are compared with the 180 case using the metric

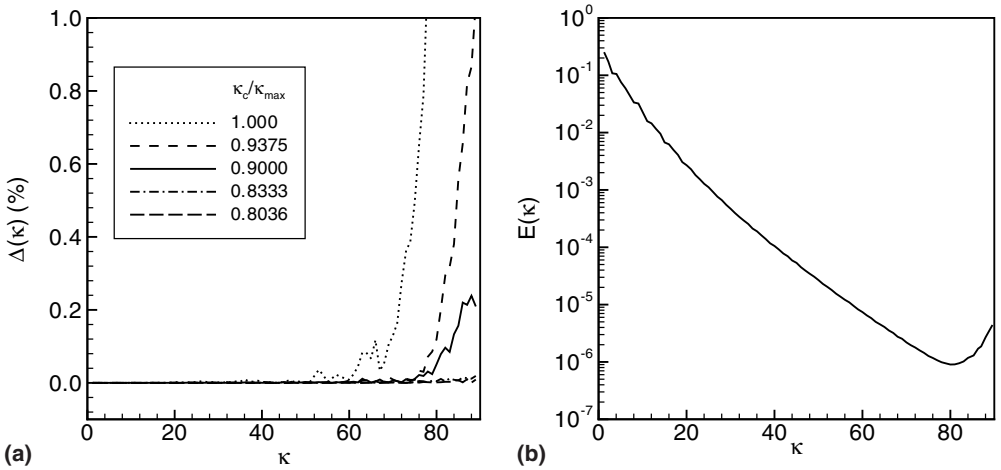

Fig. 4. Normalized differences in the velocity spectra for simulations with $r = 10$, $Re_\ell = 158$, $k_c = 90$, and various values of k_{max} (left panel). Velocity spectra at $t = 1.25$ for $k_c/k_{max} = 0.46875$ (right panel).

$$\Delta(\kappa) = \frac{|E_{180}(\kappa) - E(\kappa)|}{E_{180}(\kappa)}, \tag{28}$$

where κ is the magnitude of the three-dimensional wave number vector, $E_{180}(\kappa)$ is the three-dimensional velocity spectrum for case with $k_{max} = 180$ at $t = 1.25$ and $E(\kappa)$ is the same quantity for the case being evaluated. Test results are plotted in Fig. 4.

Evident in the plot is that aliasing errors are significant when no filter is applied, i.e., when the dealiasing filter ratio $r_d = k_c/k_{max} = 1.0$. As r_d is reduced, aliasing errors are restricted to a narrowing range of wave numbers until errors are negligible for all wave numbers when $r_d < 0.7$. The velocity spectra for the cases with $r_d = 0.5$ and $r_d = 0.46875$ are identical to seven significant digits which confirms the analytically derived 1/2 rule.

It is concluded from these tests that r_d in the range of 0.7–0.8 is sufficient to remove virtually all the aliasing errors from all wave numbers. We suggest that a less restrictive filter can be used, however, because the highest wave numbers in the simulation are not accurate anyway. This can be seen from the plot of the velocity spectrum at $t = 1.25$ for $r_d = 0.46875$ in the right-hand panel of Fig. 4. The small turn-up at high wave numbers has traditionally been attributed to spectral blocking, i.e., aliasing [54] but the simulation in this case has been shown both analytically and numerically to be free from aliasing errors. Similar turn-ups not due to aliasing errors have been observed in simulations of constant density turbulence, e.g., [42], and they are due to truncation not aliasing. Consider a simulation of decaying isotropic homogeneous turbulence that is very well resolved by the criteria of Eswaran and Pope [45], e.g., say $k_{max}\eta_k = 3$. There will be some mean transfer rate of kinetic energy from the large to the small scales, and the dissipation rate of kinetic energy will be slightly greater than the transfer rate. If k_{max} is now changed so that $k_{max}\eta_k = 2$ (still well resolved), the transfer rate will be almost unchanged and the dissipation scales will adjust in order to dissipate the same amount of energy as in the $k_{max}\eta_k = 3$ case, i.e., both simulations are well resolved and predict the same kinetic energy as a function of time. Since the dissipation rate is equal to the integral of the dissipation rate spectrum, and this integral will be the same for both simulations despite the limits of integration being different in the two cases, the two dissipation rate spectra will have to diverge above some wave number in order that the integrals be the same. In a simulation that is well resolved, the energy and dissipation rate associated with the turn up is very small, but even for simulations that are extraordinarily well resolved. the turn up will be evident if the common practice of plotting the spectra on a log scale is followed. Taking into account that the highest few wave numbers in a simulation will be affected by this truncation error, a less severe dealiasing filter can be justified than is required to make aliasing errors negligible in all wave numbers. Comparing the left-hand and right-hand panels of Fig. 4, we see that $r_d = 0.9$ is sufficient to remove aliasing effects from all wave numbers not already affected by truncation. This is the same result reported by Sandoval [25].

5.4. Temporal accuracy and stability

In the algorithm, a fractional step method involving a third-order predictor–corrector scheme with first-order pressure projection is used to advance the solution in time. Citing unpublished work by Temam, Perot [39] shows that such an algorithm will have third-order global truncation error in time when applied to the constant density case with periodic boundary conditions. Similar analysis predicts that the algorithm will be third-order accurate for the VDZM case, too. This was verified to be the true by running the V1 simulation with four different values of Δt and observing the errors in the kinetic energy at a given value t. The reference value for computing the error in kinetic energy was determined by extrapolation of the available data to $\Delta t = 0$. The results, shown in Fig. 5 indicate that the algorithm is indeed third-order accurate in time.

Given the Temam–Perot conclusion that the temporal accuracy of a simulation with periodic boundary conditions will not be affected by the order of accuracy of the pressure projection step, we have some latitude in addressing the stability issues, first identified by McMurtry [38], resulting from the manner in which $R_\rho^{\mathscr{P}} = \partial\rho/\partial t|^{\mathscr{P}}$ is predicted. Analysis of the current simulation results shows that zeroth-order extrapolation is not a good assumption most of the time, and so we consider schemes of first-order global accuracy or better. In the current implementation of the VDZM algorithm, we have available R_ρ at three earlier times without incurring an additional storage requirement just for the projection step. Therefore, the highest-order extrapolation scheme available is

$$R_\rho^{\mathscr{P}} = 3R_\rho^n - 3R_\rho^{n-1} + R_\rho^{n-2} + \mathscr{O}(\Delta t)^3. \tag{29}$$

Unfortunately, tests with the V1 case show that this extrapolation method causes the overall VDZM scheme to be unstable even for extremely small time steps.

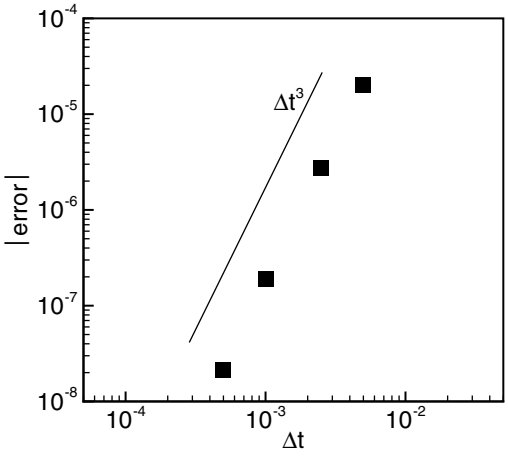

Fig. 5. Temporal convergence of the kinetic energy error.

In addition to the second-order scheme, there is a family of first-order extrapolation schemes:

$$R_\rho^{\mathscr{P}} = 2R_\rho^n - R_\rho^{n-1} + \alpha(R_\rho^n - 2R_\rho^{n-1} + R_\rho^{n-2}) + \mathscr{O}(\Delta t)^2 = aR_\rho^n + bR_\rho^{n-1} + cR_\rho^{n-2} + \mathscr{O}(\Delta t)^2, \quad (30)$$

where α is a free parameter that can be adjusted to improve the stability of the simulation and where the values of a, b, c depend on α and are introduced to simplify the discussion that follows. At this point there is no way to proceed analytically without assuming a functional form for $R_\rho(t)$. We can proceed heuristically, however, by noting that when $\alpha = 1$, (30) goes over to the (unstable) second-order extrapolation, and when $\alpha > 1$ then $|b| > |a|$, which, not unexpectedly, leads to instabilities during tests of the V1 case. Also, when $\alpha = 0$ then $c = 0$ and the scheme is unstable for case V2 unless the time step is significantly reduced. These results suggest that, if a stable scheme exists, it will have $|a| > |b| > |c|$ and $c \neq 0$ in order to combine the stabilizing effect of making R_ρ^n the dominant term and the damping effect of including R_ρ^{n-2}. It happens that if the second-order Adams–Bashforth scheme is used to approximate ρ at each time in the one-sided finite-difference formula used by Najm et al. [26] to compute $R_\rho^{\mathscr{P}}$ from stored values of ρ, i.e.,

$$\left.\frac{\partial \rho}{\partial t}\right|^{\mathscr{P}} = \frac{1}{2\Delta t}(3\rho^{\mathscr{P}} - 4\rho^n + \rho^{n-1}) \quad (31)$$

then (30) with $\alpha = 1/4$ results. Tests of cases V1 and V2 with $0 < \alpha < 0.5$ indicate that the scheme is stable and satisfies global conservation checks for the largest time step when $\alpha = 0.1$. This value of α results in (14).

5.5. Variable timestepping

When simulating flows that are changing rapidly in time, it is often advantageous to use a variable time step that can be adjusted based on flow conditions. For the current scheme, the predictor and corrector steps for ρ using variable time steps are

$$\rho^{\mathscr{P}} = \rho^n + \frac{\Delta t^n}{2}\left(\frac{\Delta t^n + 2\Delta t^{n-1}}{\Delta t^{n-1}}R_\rho^n - \frac{\Delta t^n}{\Delta t^{n-1}}R_\rho^{n-1}\right), \quad (32)$$

$$\rho^{n+1} = \rho^{\mathscr{P}} + \frac{\Delta t^n}{6}\left(\frac{2\Delta t^n + 3\Delta t^{n-1}}{\Delta t^n + \Delta t^{n-1}}R_\rho^{\mathscr{P}} + \frac{\Delta t^n + 3\Delta t^{n-1}}{\Delta t^{n-1}}R_\rho^n - \frac{\Delta t^2}{\Delta t^{n-1}(\Delta t^n + \Delta t^{n-1})}R_\rho^{n-1}\right), \quad (33)$$

and the extrapolation step to predict $R_\rho^{\mathscr{P}}$ is

$$R_\rho^{\mathscr{P}} = \frac{\Delta t^n + \Delta t^{n-1}}{\Delta t^{n-1}}R_\rho^n - \frac{\Delta t^n}{\Delta t^{n-1}}R_\rho^{n-1} + \frac{\alpha}{3}\left[\frac{\Delta t^n + \Delta t^{n-1} + \Delta t^{n-2}}{\Delta t^{n-1} + \Delta t^{n-2}}R_\rho^n - \frac{\Delta t^n + \Delta t^{n-1} + \Delta t^{n-2}}{\Delta t^{n-2}}R_\rho^{n-1} + \left(\frac{\Delta t^n + \Delta t^{n-1}}{\Delta t^{n-2}} - \frac{\Delta t^n}{\Delta t^{n-1} + \Delta t^{n-2}}\right)R_\rho^{n-2}\right]. \quad (34)$$

6. Results

6.1. Kinetic energy

Sandoval [25] investigated flow configurations similar to those discussed in this paper, but with a maximum density ratio of 4.0. He noted that the evolution of the average kinetic energy, $K = \langle 1/2\rho u_i u_i \rangle$, was almost the same in simulations with constant density and with $r = 4$ provided that ρ and u_i were not correlated. It was postulated that a difference in the decay rate might be observed if the density ratio were sufficiently high. In Fig. 6, K normalized by K_0, its value at $t = 0$, is shown versus time for the cases listed in Table 1. It is apparent that the decay rates for the three cases with the same nominal Reynolds number (C2, V1 and V2) are almost identical. The constant density case with higher initial Reynolds number (C3) decays more slowly initially but adjusts to approximately the same

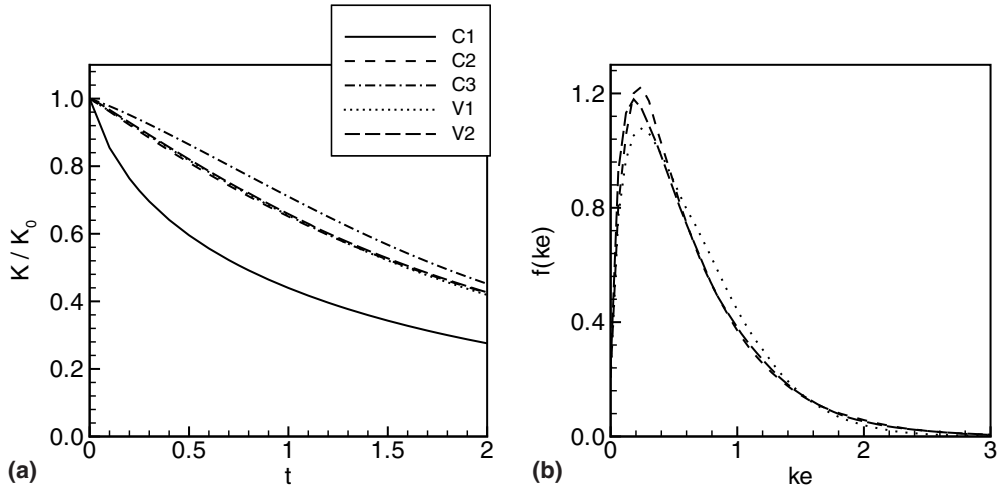

Fig. 6. Time evolution of average kinetic energy (left panel). Probability density of kinetic energy at $t = 2$ (right panel).

decay rate by $t = 0.5$. Similarly, the low Reynolds number constant density case (C1) adjusts fairly quickly to about the same decay rate.

These results are a reflection of the fact that isotropic homogeneous turbulence decays in quasi-equilibrium so that, to a good approximation, the average dissipation rate of kinetic energy is equal to the average transfer rate of energy from the large to the small scales. This transfer rate is related to the correlation between ρ, u_i, and u_j, which is unaffected by density ratio if the density and velocity are not correlated. As a result, no dependence on r is observed in the current simulation results shown in Fig. 6. The initial condition is in quasi-equilibrium for $Re_\ell = 158$, so cases C1 and C3 decay at different rates than the other cases at early time until quasi-equilibrium is restored.

Since the flow is statistically isotropic and homogeneous, and since ρ and u_i are uncorrelated, limited insight can be gained from these simulations about the mean energetics of variable density turbulence. Indeed, for this flow configuration, not only is the evolution of average kinetic energy approximately independent of r, the evolution of the probability density of the local kinetic energy, ke, is also nearly independent of r as shown in the right-hand panel of Fig. 6. It may be that density gradients do not significantly affect flow energetics unless the density and velocity fields are correlated, or it may be that the flow configuration considered in this paper is not well suited for studying flow energetics.

7. Conclusions

Direct numerical simulations are potentially a valuable tool for studying variable density turbulence at zero Mach number. Previous numerical investigations of this flow regime have been hampered by numerical instabilities in the pressure projection step. The algorithm presented here overcomes the instability problem, at least for density ratios up to 35. In pseudo-spectral schemes, if the spatial resolution is adequate for the conservation equations for mass, momentum, and mechanical energy to balance, then the simulations will be adequately dealiased if $k_c/k_{\max} \leqslant 0.9$. In addition, failure of a simulation to conserve mass to machine precision is a strong predictor of a numerical instability. Finally, it is observed that density ratio has little effect on the mean energetics of isotropic homogeneous turbulence, but it is not clear if this an artifact of the flow configuration of if the result can be applied to more general flows.

Acknowledgments

The authors thank Professor J.B. Perot for his insight into to the algorithm proposed in this paper, and Dr. V. Nilsen and Professor G. Kosály for the use of their initial velocity fields. The Arctic Region Supercomputing Center provided high performance computing (HPC) resources for the larger simulations. The remaining simulations were computed in-house on a cluster computer purchased under Office of Naval Research Grant No. N00014-00-1-0449.

References

[1] Brown GL, Roshko A. On density effects and large structures in turbulent mixing layers. J Fluid Mech 1974:775–816.
[2] Lele SK. Flows with density variations and compressibility: similarities and differences. In: Fulachier L, Lumley JL, Anselmet F, editors. IUTAM symposium on variable density low-speed turbulent flows. Proceedings of the IUTAM symposium held in Marseille, France, 8–10 July, 1996. Dordrecht: Kluwer; 1997. p. 279–301.
[3] Bellan J. Supercritical fluid behavior and modeling: drops, streams, shear and mixing layers, jets and sprays. Prog Energy Combust Sci 2000;26:329–66.
[4] Pope SB. Turbulent flows. Cambridge: Cambridge University Press; 2000.
[5] Orszag SA, Patterson GS. Numerical simulation of turbulence. In: Rosenblatt M, Van Atta C, editors. Statistical models and turbulence. Lecture notes in physics, vol. 12. New York: Springer; 1972. p. 127–47.
[6] Herring JA. Approach of axisymmetric turbulence to isotropy. Phys Fluids 1974;30:859.
[7] Schumann U, Patterson GS. Numerical study of return of axisymmetric turbulence to isotropy. J Fluid Mech 1978;33:711.
[8] Riley JJ, Metcalfe RW, Weissman MA. Direct numerical simualtions of homogeneous turbulence in density stratified flows. In: West BJ, editor, Proc AIP conf nonlinear properties of internal waves; 1981. p. 79–112.
[9] Deardorff JW. Three-dimensional numerical study of the height and mean structure of a heated planetary boundary layer. Blm 1974;7:81.
[10] Riley JJ, Metcalfe RW. Direct numerical simulations of the turbulent wake of an axisymmetric body. In: Andre J-C, Cousteix J, Durst F, Launder B, Schmidt F, Whitelaw J, editors. Turbulent shear flows, vol. 2. Berlin: Springer; 1980. p. 78.
[11] Martin MP, Candler GV. Effect of chemical reactions on decaying isotropic turbulence. Phys Fluids 1998;10:1715–24.
[12] Cook AW, Riley JJ. Direct numerical simulation of a turbulent reactive plume on a parallel computer. Jcp 1996;129:263–83.
[13] Meneveau C, Poinsot T. Stretching and quenching of flamelets in premixed turbulent combustion. Combust Flame 1991;86:311–32.
[14] Vervisch L, Poinsot T. Direct numerical simulation of non-premixed turbulent flames. In: Lumley JL, Van Dyke M, Reed HL, editors. Annual review of fluid mechanics, vol. 30. Palo Alto, CA: Annual Reviews, Inc.; 1998. p. 655–91.
[15] Huang PG, Coleman GN, Bradshaw P. Compressible turbulent channel flows: DNS results and modelling. J Fluid Mech 1995;305:185–218.
[16] Coleman GN, Kim J, Moser RD. A numerical study of turbulent supersonic isothermal-wall channel flow. J Fluid Mech 1995;305:159–83.
[17] Guarini SE, Moser RD, Shariff K, Wray A. Direct numerical simulation of a supersonic turbulent boundary layer at mach 2.5. J Fluid Mech 2000;414:1–33.
[18] Maeder T, Adams NA, Kleiser L. Direct simulation of turbulent supersonic boundary layers by an extended temporal approach. J Fluid Mech 2001;429:187–216.
[19] Pantano C, Sarkar S. A study of compressibility effects in the high-speed turbulent shear layer using direct simulation. J Fluid Mech 2002;451:329–71.
[20] Freund JB, Lele SK, Moin P. Compressibility effects in a turbulent annular mixing layer. Part 1. Turbulence and growth rate. J Fluid Mech 2000;421:229–67.
[21] Freund JB, Moin P, Lele SK. Compressibility effects in a turbulent annular mixing layer. Part 2. Mixing of a passive scalar. J Fluid Mech 2000;421:269–92.

[22] Klainerman S, Majda A. Compressible and incompressible fluids. Commun Pur Appl Math 1982;35:629–51.
[23] McMurtry PA, Jou W-H, Riley JJ, Metcalfe RW. Direct numerical simulations of a reacting mixing layer with chemical heat release. Aiaaj 1986;24:962.
[24] McMurtry PA, Riley JJ, Metcalfe RW. Effects of heat release on the largescale structures in turbulent mixing layers. J Fluid Mech 1989;199:297–332.
[25] Sandoval DL. The dynamics of variable-density turbulence. Ph.D. thesis, University of Washington; 1995.
[26] Najm HN, Wyckoff PS, Omar MK. A semi-implicit numerical scheme for reacting flow. Jcp 1998;143:381–402.
[27] Cook AW, Dimotakis PE. Transition stages of Rayleigh–Taylor instability between miscible fluids. J Fluid Mech 2001;443:69–99.
[28] Djeridane T, Amielh M, Anselmet F, Fulachier L. Velocity turbulence properties in the near-field region of axisymmetric variable density jets. Phys Fluids 1996;8:1614–30.
[29] Panchapakesan NR, Lumley JL. Turbulence measurements in axisymmetrical jets of air and helium. 1. Air-jet. J Fluid Mech 1993;246:197–223.
[30] Panchapakesan NR, Lumley JL. Turbulence measurements in axisymmetrical jets of air and helium. 2. Helium jet. J Fluid Mech 1993;246:225–47.
[31] Sautet JC, Stepowski D. Evolution of the effective nozzle diameter in the buoyancy free development of turbulent jets with variable density. Exp Fluids 1998;25:280–2.
[32] Favre-Marinet M, Camano EB, Sarboch J. Near-field of coaxial jets with large density differences. Exp Fluids 1999;26:97–106.
[33] Riva R, Binder G, Favremarinet M, Harion JL. Development of turbulent boundary-layer with large density gradients. Exp Therm Fluid Sci 1994;9:165–73.
[34] Harion JL, Favre-Marinet M, Binder G. Density and velocity measurements in turbulent He–air boundary layers. Exp Therm Fluid Sci 1997;14:92–100.
[35] Gottlieb D, Orszag SA. Numerical analysis of spectral methods: theory and applications. NSF-CBMS, regional conference series in applied mathematics, vol. 26. Philadelphia: Society of Industrial and Applied Mathematics; 1977.
[36] Shih TS, Lumley JL, Janicka JL. Second order modeling of a variable density mixing layer. J Fluid Mech 1987;180:93–116.
[37] Chassaing P, Harran G, Joly L. Density fluctuation correlations in free turbulent binary mixing. J Fluid Mech 1994;279:239–78.
[38] McMurtry PA. Direct numerical simulations of a reacting mixing layer with chemical heat release. Ph.D. thesis, University of Washington; 1987.
[39] Perot JB. An analysis of the fractional step method. J Comput Phys 1993;108:51–8.
[40] Nilsen V, Kosály G. Differentially diffusing scalars in turbulence. Phys Fluids 1997;9(11):3386–97.
[41] Mell WE, Nilsen V, Kosály G, Riley JJ. Direct numerical simulation investigation of the conditional moment closure model for nonpremixed turbulent reacting flows. Combust Sci Technol 1993;91:179–86.
[42] de Bruyn Kops SM, Riley JJ. Direct numerical simulation of laboratory experiments in isotropic turbulence. Phys Fluids 1998;10(9):2125–7.
[43] Wang H, George W. The integral scale in homogeneous isotropic turbulence. J Fluid Mech 2002;459:429–43.
[44] Sandoval DL, Clark TT, Riley JJ. Buoyancy-generated variable-density turbulence. In: Fulachier L, Lumley JL, Anselmet F, editors. IUTAM symposium on variable density low-speed turbulent flows. Proceedings of the IUTAM symposium held in Marseille, France, 8–10 July, 1996. Dordrecht: Kluwer; 1997. p. 173–80.
[45] Eswaran V, Pope S. Direct numerical simulations of the turbulent mixing of a passive scalar. Phys Fluids 1998;31:506.
[46] Orszag S. On the elimination of aliasing in finite difference schemes by filtering high-wavenumber components. J Atmos Sci 1971;28:1074.
[47] Patterson Jr GS, Orszag SA. Spectral calculation of isotropic turbulence: efficient removal of aliasing interaction. Phys Fluids 1971;14:2538–41.
[48] Rogallo RS. An ILLIAC program for the numerical simulation of homogeneous, incompressible turbulence. Tech Rep TM-73203, NASA; 1977.
[49] Rogallo RS. Numerical experiments in homogeneous turbulence, Tech. Rep. TM-81315, NASA; 1981.
[50] Rogallo RS, Moin P. Numerical simulation of turbulent flows. Arfm 1984;16:99–137.
[51] Kerr RM. Higher-order derivative correlations and the alignment of smallscale structures in isotropic turbulence. J Fluid Mech 1985;153(31):31.
[52] Zang T. On the rotation and skew-symmetric forms for incompressible flow simulations. Applied Numerical Mathematics 1991;7:27–40.
[53] Blaisdell GA, Spyropoulos ET, Qin JH. The effect of the formulation of nonlinear terms on aliasing errors in spectral methods. Appl Numer Math 1996;21(3):207–19.
[54] Boyd JP. Chebyshev and Fourier spectral methods. New York: Dover; 2001.